2026 IEEE International Conference on Robotics and Automation (ICRA 2026)
June 1-5, 2026. Vienna, Austria

Tactile-Proprioceptive Sensor Fusion for Contact Wrench Estimation in Whole-Body Physical Human-Robot Interaction

Junha Min, Junghyeon Ma, Jiwung Kwon, Sunggyu Bae, Joohyung Kim, and *Kyungseo Park

Abstract— **Direct physical guidance is a natural means of teaching and interacting with robots, and robotic skins make a key contribution by enabling sensitive contact sensing and localization. This paper presents a tactile–proprioceptive sensor fusion framework for natural physical human-robot interaction. Tactile cues from pneumatic skin pads serve as contact indicators that bypass the ambiguity between frictional residues and applied external forces, enabling highly sensitive contact detection without explicit friction identification. We fuse these cues with motor-current–based proprioception to reconstruct multi-axis contact forces on the robot surface. To maintain accuracy during motion, we employ a temporal convolutional network (TCN) to mitigate friction hysteresis during stick–slip transitions, reducing uncertainty at contact onset and yielding smooth, responsive guidance. We validate the approach on a skin-integrated robot arm: (i) multi-axis forces are reconstructed in stationary contacts, and (ii) simultaneous force estimation and kinesthetic teaching are demonstrated. Results indicate improved sensitivity and responsiveness across diverse contact conditions compared with tactile-only and proprioceptive-only baselines, supporting tactile–proprioceptive fusion as a reliable pathway to safe, intuitive physical human–robot interaction.**

I. INTRODUCTION

In human–robot interaction, teaching robots through direct physical guidance is regarded as one of the most intuitive approaches. To enable this, reliable perception of physical contact is essential, and numerous approaches to external force estimation have been proposed [1], [2].

Force/torque (F/T) sensors and joint torque sensors have been used for direct measurement of external forces. While these devices provide accurate measurements, they present several drawbacks, including high cost, susceptibility to damage from external impacts, and reductions in the robot's structural stiffness [3]–[6]. As an alternative, many studies estimate joint torques and external forces from motor currents in conjunction with a dynamic model [7]. This proprioceptive approach improves durability and accessibility by avoiding additional sensors. However, significant errors arise from motor friction and hysteresis, especially in stationary and quasi-static regimes [8].

To mitigate this issue, larger thresholds are typically introduced to distinguish external forces from model errors. This method is intuitive and simple but effectively introduces a dead band, which degrades the robots' contact responsiveness. To move beyond ad-hoc thresholding, several studies have leveraged signal-processing methods, such as Kalman filtering, to compensate for friction-induced hysteresis [9], [10]. More recently, data-driven approaches using artificial neural networks have been explored to learn the nonlinear hysteresis patterns and reduce residual errors [11]–[13].

In parallel, whole-body robot skins have been considered a promising solution because they enable high-sensitivity contact detection and localization across the robot's entire surface [14]–[16]. Such systems should provide not only tactile sensing but also passive safety via mechanical compliance. For instance, pneumatic robot skins provide passive safety through a compliant, impact-absorbing envelope, while internal pressure changes under external loads enable tactile sensing [17]. Moreover, combining mechanical compliance with tactile feedback has enabled safe whole-body manipulation using simple control strategies [18]. 3D printing has also been leveraged to implement low-cost and easy-to-build skins, and associated interaction frameworks have been demonstrated [19]. Nonetheless, individual skin pads provide only the magnitude of contact force, usually the normal component.

To address this limitation, sensor-fusion methods that combine joint-torque measurements with robot-skin tactile sensing have been proposed [20]–[22]; however, factors such as cost and scalability have not been adequately addressed.

In this paper, we propose a hybrid tactile-proprioceptive approach that combines motor-current measurements with pneumatic robot skins for natural interaction. The main contributions are as follows:

1) Using tactile signals as contact cues, we disambiguate static-friction residuals from true external forces, enabling sensitive force perception and agile responses.
2) By fusing tactile cues with proprioceptive sensing, we reconstruct physical interactions as a multi-axis force vector defined on the robot's surface.
3) We train a temporal convolutional network (TCN) that models friction from quasi-static residuals and compensates it online. By integrating with the above components, it substantially reduces the dead band and enables a natural, intuitive kinesthetic teaching framework.

The remainder of this paper is organized as follows: Section II reviews robot dynamics and external-force estimation. Section III describes the hardware setup, including manipulator and robot skin modules. Section IV presents the proposed sensor-fusion strategy and the TCN-based residual compensator. Section V presents the experiments and demon-

J. Min, Junghyeon Ma, Jiwung Kwon, Sunggyu Bae and K. Park are with the Department of Robotics and Mechatronics Engineering, DGIST (Daegu Gyeongbuk Institute of Science and Technology), Daegu 42988, Republic of Korea

J. Kim is with the Kinetic Intelligent Machine Lab (KIMLAB), University of Illinois Urbana-Champaign, Champaign, Illinois 61801, USA

*Corresponding authors: kspark@dgist.ac.kr

stration. Finally, Section VI concludes with limitations and direction for future work.

II. SYSTEM DYNAMICS MODELING

A. Robot Dynamics

For an n-degree-of-freedom (DoF) rigid robot, the joint-space dynamics are written as

$$\tau_{dyn} = M(q)\ddot{q} + C(q,\dot{q})\dot{q} + G(q) \tag{1}$$

where $q, \dot{q}, \ddot{q} \in \mathbb{R}^n$ denote the joint position, velocity, and acceleration vectors. The terms $M(q) \in \mathbb{R}^{n\times n}$, $C(q,\dot{q}) \in \mathbb{R}^{n\times n}$, and $G(q) \in \mathbb{R}^n$ represent the inertia matrix, Coriolis and centrifugal matrix, and gravity vector, respectively. τ_{dyn} is the inverse-dynamics torque, so the joint-side actuator torque τ is written as

$$\tau = \tau_{ext} + \tau_{dyn} + \tau_{fric} + \tau_{error} \tag{2}$$

where τ_{ext} the torque induced by external contacts, τ_{fric} the internal friction torque, and τ_{error} aggregates modeling error and measurement noise.

The task-space external wrench $F_{ext} \in \mathbb{R}^6$ and the corresponding joint-space external torque τ_{ext} are related via the Jacobian $J(q)$:

$$\tau_{ext} = J(q)^T F_{ext}. \tag{3}$$

The geometric Jacobian $J(q)$ in (3), which relates joint velocities to the contact point velocity, is computed from the joint origins P_i, rotation axes z_i, and the contact point P_{contact}, all expressed in the base frame $\{0\}$. The contact point P_{contact} can be defined by introducing an additional frame estimated from tactile sensor measurements. For a revolute joint i, the corresponding Jacobian column $[J_{v,i}^T, J_{w,i}^T]^T$ is given by the standard formulation.

$$J_{v,i} = z_i \times (P_{\text{contact}} - P_i), \quad J_{w,i} = z_i \tag{4}$$

where $J_{v,i}$ and $J_{w,i}$ represent the linear and angular velocity contributions. The resulting Jacobian is then transformed to the local contact frame using the rotation matrix R_{contact}.

B. Friction Models

In contrast to the dynamics model, friction is highly sensitive to various physical properties, making its modeling more challenging. Accurate identification of τ_{fric} is thus essential for the precise estimation of the external torque τ_{ext}.

A commonly used static friction model combines Coulomb friction τ_c, viscous τ_v, and Stribeck effects:

$$\tau_{fric}(\dot{q}) \;=\; \Big[\tau_c + (\tau_s - \tau_c)\exp\Big(-\Big|\frac{\dot{q}}{\dot{q}_s}\Big|^{\delta}\Big)\Big]\,\mathrm{sgn}(\dot{q}) \;+\; b\,\dot{q} \tag{5}$$

where τ_s is the static level, $b > 0$ the viscous coefficient (equivalently $\tau_v(\dot{q}) \triangleq b\,\dot{q}$), $\dot{q}_s > 0$ the Stribeck velocity scale, and $\delta > 0$ a shape parameter.

For high-reduction actuators (ratio $\approx$ 500:1) used in this study, the internal contact forces in the transmission scale significantly with the applied load, directly influencing friction dynamics. To account for this, the constant friction coefficients in (5) are modified to include load-dependent functions [23]:

$$\tau_{c,load} = \tau_c + \alpha_c|G(q)|, \quad b_{load} = b + \alpha_v|G(q)| \tag{6}$$

where $\tau_{c,load}$ and b_{load} denote the load-dependent Coulomb and viscous friction coefficients, and $\alpha_c, \alpha_v \geq 0$ are scaling constants characterizing load dependence. Here we use $|G(q)|$ as a proxy for load; this approximation is acceptable because the robot links are the primary source of load, whereas pHRI interaction forces were assumed to be gentle in typical physical guidance.

While the aforementioned friction models describe motor friction reasonably well, they do not capture the complex dynamics, including stick-slip motion and nonlocal memory hysteresis. Although advanced models like LuGre [24] or Generalized Maxwell-Slip (GMS) [25] address these phenomena, they require identifying a large number of parameters and are sensitive to environmental changes.

To this end, we avoid complex physical modeling and employ a friction dynamics model based solely on (5) and (6). Instead, we leverage tactile information to compensate for frictional hysteresis, effectively bypassing the intricate parameter identification process as detailed in the following sections.

III. SKIN-INTEGRATED ROBOT ARM

A. Manipulator

We conducted our study using a serial manipulator integrated with pneumatic robot skin. The platform is a conventional elbow-type manipulator [26]. To enable more natural motion, we added a new actuator on the proximal link whose rotational axis is coaxial with the link's longitudinal axis. The wrist joint was removed to simplify system identification and emphasize whole-body interaction. As a result, our setup has four DoFs at the forearm, as illustrated in Fig. 1(a).

Each joint is actuated by a servo motor with a cycloidal gear reduction of approximately 500:1 (DYNAMIXEL-P PH54 series, Robotis). The motors use a 24 V supply power and communicate with peers and the host through an RS-485 daisy chain. The communication cycle was nearly 400 Hz, so motor state variables and configuration parameters (e.g., control gains) can be exchanged in real-time.

B. Pneumatic Robot Skin

We adopted the pneumatic robot skin framework proposed in our previous work [19] and customized it for the manipulator, as shown in Fig. 1(b). Each skin pad was 3D-printed (FDM-type) from flexible TPE (eLastic, eSUN) and chemically smoothed with tetrahydrofuran (THF) to achieve air-tight surface. Each pad has a barbed port and was connected via silicone tubing to an air-pressure sensor (HSCDANT005PGAA5, Honeywell) placed inside the robot. The sensor outputs 0 – 3.3 V in proportion to the applied air pressure, and microcontroller board (Teensy 4.0, PJRC) reads those values in real-time.

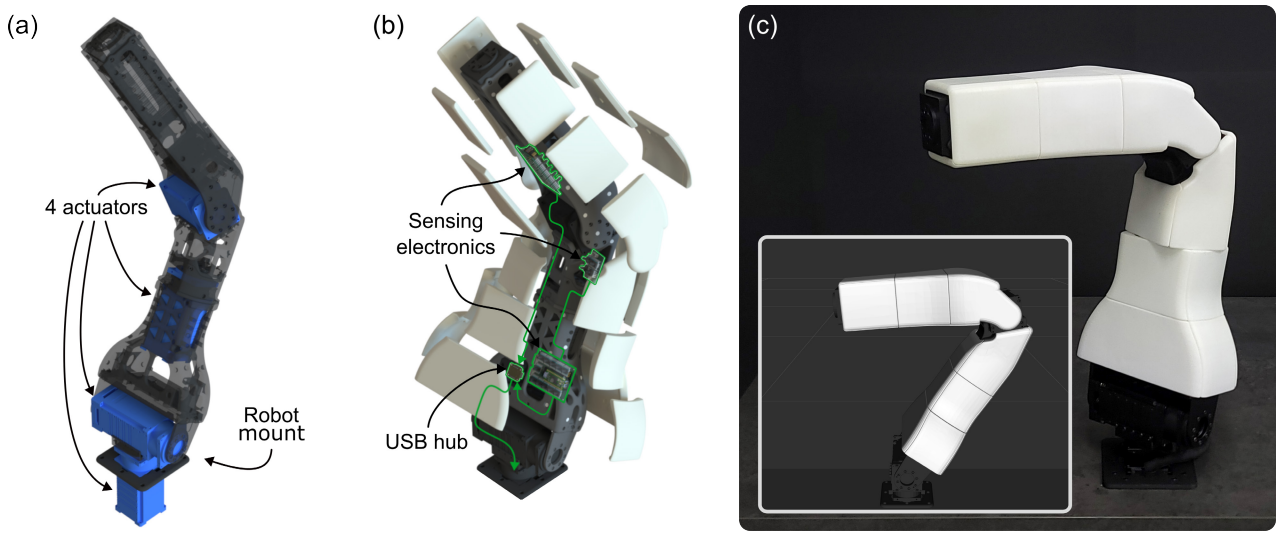

Fig. 1. Skin-integrated robot arm. (a) Kinematic structure and actuator layout of the manipulator. (b) Pneumatic skin design and sensing electronics connections. (c) Photograph of the skin-integrated robot arm and its RViz visualization.

The microcontroller handled low-level signal processing (e.g., low-pass filtering, contact thresholding) and data transmission. Data were formatted as arrays and sent to the host's ROS 2 network via micro-ROS with a publishing rate of 1 kHz.

The pneumatic robot skin was sensitive to small external forces, and its bandwidth exceeded that of motions from typical pHRI scenarios, enabling diverse interactions from basic teaching to gesture-based commanding [19]. However, within a single pad, contact localization was not possible and only the normal force could be measured. Moreover, for the same applied force, the pressure reading varied with contact area and geometry. These limitations impose significant constraints on tactile-only approach and motivate complementary hybrid with proprioception.

IV. SENSOR FUSION

In robotic systems, the measured torque τ_{meas} is typically decomposed into several components, as shown in Equation (7). This measured torque is often estimated from the motor current I, and a torque constant K_t via Equation (8).

$$\tau_{meas} = \tau_{dyn} + \tau_{fric} + \tau_{res} \tag{7}$$

$$\tau_{meas} = K_t I. \tag{8}$$

Here, the torque residual τ_{res} in Equation (7) comprises not only the external torque τ_{ext} but also inherent modeling errors and complex frictional behavior not captured by nominal model. These unmodeled effects include static friction and stick–slip transitions under static and quasi-static conditions. Such friction components exhibit strong hysteresis dependency, which makes their analytical modeling exceptionally challenging and complicates the accurate estimation of τ_{ext}.

To address this issue, this paper proposes two methods. First, we use tactile signals to estimate static friction and to infer external forces under static conditions. Second, we introduce a learning-based method that handles uncertainty at the static-to-kinetic transition, enabling more natural motion in pHRI tasks such as kinesthetic teaching.

A. Contact-aware Torque Estimation

We propose a method that leverages tactile data to disambiguate static friction from external torque. Under static conditions ($\dot{q} = 0$), the torque residual is modeled as the sum of static friction $\tau_{fric,s}$ and external torque τ_{ext}:

$$\tau_{res} \;=\; \tau_{fric,s} \;+\; \tau_{ext}. \tag{9}$$

Using tactile signals, we can detect the physical contact and its onset time t_{on}, and define the pre-contact baseline $\tau_{res}(t_{on}^{-})$. We then compute the increment of the residual:

$$\Delta\tau_{res}(t) \;=\; \tau_{res}(t) \;-\; \tau_{res}(t_{on}^{-}). \tag{10}$$

Here, we can assume that the pre-contact baseline $\tau_{res}(t_{on}^{-})$ can be attributed exclusively to friction.

$$\hat{\tau}_{fric,s} \;=\; \tau_{res}(t_{on}^{-}). \tag{11}$$

While the robot remains at rest, we assume the static-friction term is constant for small external loads such as gentle physical guidance. Consequently,

$$\hat{\tau}_{ext}(t) \;=\; \Delta\tau_{res}(t) \;=\; \Delta\tau_{meas}. \tag{12}$$

In this way, we could estimate the torque due to external forces without relying on a dynamics model. The proposed algorithm can be formalized as a finite-state machine (FSM), as shown in Fig. 2(b). Here, we consider three states:

(i) Static (without contact)
: the robot is stationary and no external contact is detected.

(ii) Static (with contact)
: a contact is detected while the system remains stationary.

(iii) Dynamic
: the robot is in motion (i.e., physical interaction).

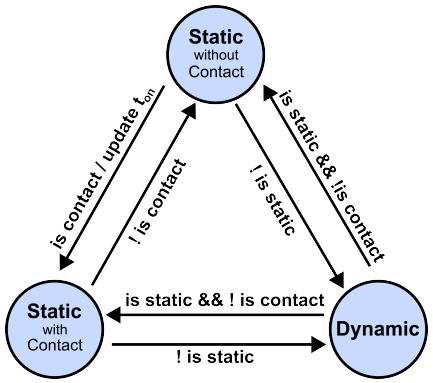

Fig. 2. Contact-aware torque estimation algorithm represented as a three-state Finite-State Machine (FSM). Transition conditions: (1) 'is contact' indicates tactile sensor activation, (2) 'is static' indicates stationary robot state, and (3) 'update t_{on}' sets the contact onset reference time.

As contact occurs, transitioning the state from (i) to (ii), these tactile cues are used to estimate the external force via Equation (12).

This approach improves responsiveness in high-gear-ratio systems, where friction introduces large uncertainty. By canceling static friction at contact onset, we can bypass the large dead-band, which is required by other methods that rely purely on motor current and a dynamics model.

However, this method is valid only in the static states (i) and (ii). Once motion is initiated by the estimated external force, Equation (12) is no longer valid. During this phase, the friction transitions from static to dynamic and exhibits trajectory-dependent hysteresis, which cannot be captured by Equation (11). Consequently, a large discontinuity arises when transitioning from state (ii) to state (iii).

B. TCN-Driven Seamless Transition Friction Compensator

Friction in the static to kinetic transition is hysteretic and nonlinear, so it cannot be fully characterized from the instantaneous kinematic states $(q, \dot{q}, \ddot{q})$ alone. To address this challenge, we propose a data-driven compensation strategy based on a Temporal Convolutional Network (TCN). The proposed model utilizes not only the time-series data of the kinematic state $q, \dot{q}, \ddot{q}$ but also the estimated static friction $\hat{\tau}_{fric,s}$ as an additional input. The estimate $\hat{\tau}_{fric,s}$, explicitly captured by the FSM via tactile cues at motion onset, provides the system with the precise initial condition for the moment of static-to-dynamic state transition. This is key information to explicitly resolve the aforementioned ambiguity, which could not be addressed using only kinematic data. By referencing this initial friction state, the TCN processes the subsequent kinematic time-series data to effectively infer the complex friction residual during the transition phase, which the conventional friction model (5) fails to estimate. The TCN is suited for efficiently learning this short-term, hysteretic data.

$$\tau_{\text{TCN}} = TCN(q, \dot{q}, \ddot{q}, \hat{\tau}_{\text{fric,s}}),\ (\hat{\tau}_{\text{fric,s}} = 0 \text{ if } \dot{q} \neq 0). \tag{13}$$

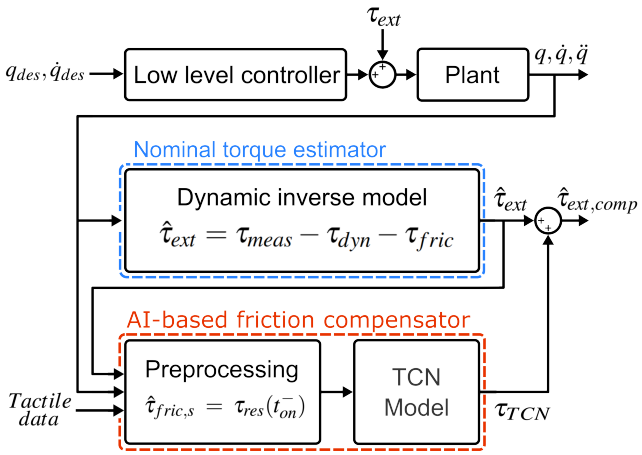

Fig. 3. Pipeline of the joint external torque estimation. An AI-based friction compensator utilizes the kinetic state, the output derived from the nominal inverse dynamics model, and tactile sensor data to compensate for static friction and friction within the transition region.

Constraining the network input to the static-friction estimate $\hat{\tau}_{fric,s}$ is crucial for inference under forced conditions. Feeding the non-disambiguated residual τ_{res} would cause the network to compensate not only friction but also external torque, thereby degrading external-torque estimation. The tactile sensing stage separates friction from external torque, ensuring that the network receives an input invariant to external forces.

To train this friction model, which is decoupled from external torque, training data was collected by driving an excitation trajectory without external contact ($\tau_{ext} = 0$). Under this condition, the measured τ_{res} corresponds to the ground-truth friction that must be compensated. Particularly, the transition friction in the static-to-dynamic regime exhibits rapidly changing, high-frequency characteristics. To enhance the learning of high-frequency characteristics, we adopted the Multi-head TCN architecture proposed in [13], which processes the residual by separating it into low- and high-frequency components.

This architecture employs a shared TCN backbone that processes the temporal input sequence through dilated convolutional layers. The feature vector from the final timestep is input to two separate linear heads that independently predict the low- and high-frequency components of the friction residual. We use a kernel size of $k = 4$ to give the model more time window, so the initial friction state still affects the estimates during the transition phase. The model is trained using a weighted combination of mean squared errors from both outputs.

The final external torque estimation of the proposed architecture is defined as follows:

$$\hat{\tau}_{ext,comp} = \tau_{meas} - (\tau_{dyn} + \tau_{fric} + \tau_{TCN}). \tag{14}$$

The complete torque estimation framework is presented in Fig. 3. The system operates at the motor communication rate to maintain synchronization between the nominal and

TABLE I. Residual analysis of models in static and static-to-kinetic states

RMSE(mA) in Static State				
Model	Joint 1	Joint 2	Joint 3	Joint 4
Nominal Dynamic	92.56	387.10	329.22	311.81
TCN Compensated	18.32	37.73	43.89	27.88
RMSE(mA) in Static-to-Kinetic State				
Model	Joint 1	Joint 2	Joint 3	Joint 4
Nominal Dynamic	125.07	333.60	349.84	275.28
TCN Compensated	85.43	119.36	175.63	118.80
Std Dev(mA) in Static State				
Model	Joint 1	Joint 2	Joint 3	Joint 4
Nominal Dynamic	92.46	384.17	329.07	311.81
TCN Compensated	18.26	37.53	43.44	27.86
Std Dev(mA) in Static-to-Kinetic State				
Model	Joint 1	Joint 2	Joint 3	Joint 4
Nominal Dynamic	125.08	329.77	349.70	275.29
TCN Compensated	85.29	119.05	175.60	118.52

TCN-based components. For robust detection, we employ a single dead-band threshold determined by the TCN estimator (14) across all conditions. While the static estimator (12) permits a lower threshold, using a unified value prevents discontinuities during state transitions and sufficiently covers the error margins of the static-to-dynamic transition.

V. EXPERIMENT AND RESULT

A. Error Analysis and Model Validation

This section quantitatively analyzes the motor torque estimation accuracy under force-free conditions for the nominal dynamic model, derived from identification-based calculation of $\tau_{dynamic}$ and τ_{fric}, and the TCN compensated model, which includes the compensation term τ_{TCN}. The error analysis calculates τ_{error} according to Eq. (2), assuming $\tau_{ext} = 0$. As the motor used in this study does not provide an official motor torque constant K_t, all torque values in the experiments are replaced by current values with the unit (mA).

Experimentally, static state data were collected when the joint velocity remained below a threshold of 0.0001 rad/s. For the static-to-kinetic transition, data were collected from the moment the velocity exceeded the threshold to the point where the residuals of both models equalized. From this analysis, an average window size of 70 ms (30 data points) was determined. The results for the RMSE and STD of the residual between the actual current value and the model are shown in Table I. In the Static state, the compensator reduced the RMSE of the current residual from the nominal model's average of 280.17 mA to 31.96 mA, an 88.6% reduction; this indicates that the static friction effect was, while not perfectly, substantially mitigated. In the static-to-kinetic transition, the average RMSE for all joints decreased from 270.95 mA to 124.81 mA, a 54.8% reduction. The standard deviation of the residual also showed similar values to the RMSE, implying that the model has low bias. Fig. 4 shows the probability density function and confidence interval for both models, and this reduction in error variance is important as it enables the setting of a smaller estimation

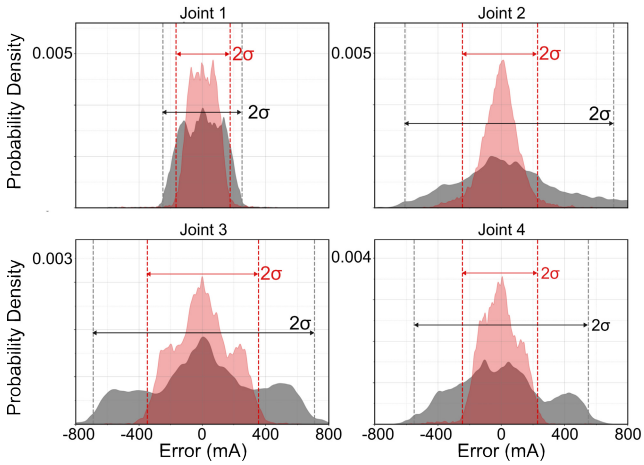

Fig. 4. Joint-wise standard deviation (STD) probability density function (PDF) in the static-to-kinetic transition region. Gray: identification-based nominal model; Red: TCN-compensated model.

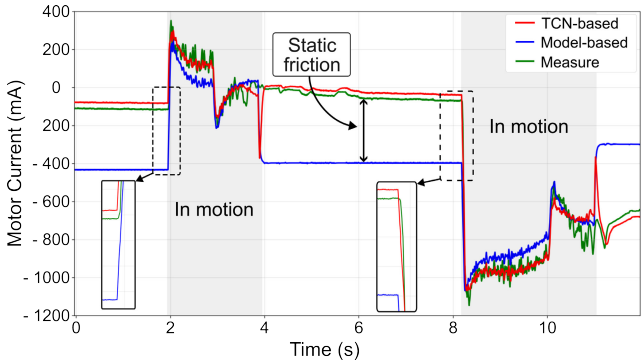

Fig. 5. Model predictions for Joint 4 during static-to-kinetic transitions. Green: measured motor current corresponding to the ground truth; Blue: identification-based model (without compensation); Red: TCN-compensated model.

dead band, allowing the system to react more sensitively to subtle external forces.

Fig. 5 compares the actual motor current with the estimates of both models for an arbitrary motion of joint 4. Throughout the stationary period, the TCN model effectively cancels the large static-friction residual present in the nominal model. Around the motion onset and termination, the TCN model produces smooth current estimates without spike-like errors by carrying over the initial friction. However, there is a estimation error immediately after stopping because $\tau_{fric,s} = 0$ during motion, the TCN's input window initially lacks stationary samples when returning to rest, causing a short mismatch until the window fills. This error is not a problem since this phase satisfies the static condition and external force estimation is still possible using Equation (12) (model free method). Additionally, performance improvements were observed during motion since the joint's kinetic state is input to the TCN; however, as this is outside the scope of this study, so we omit further analysis.

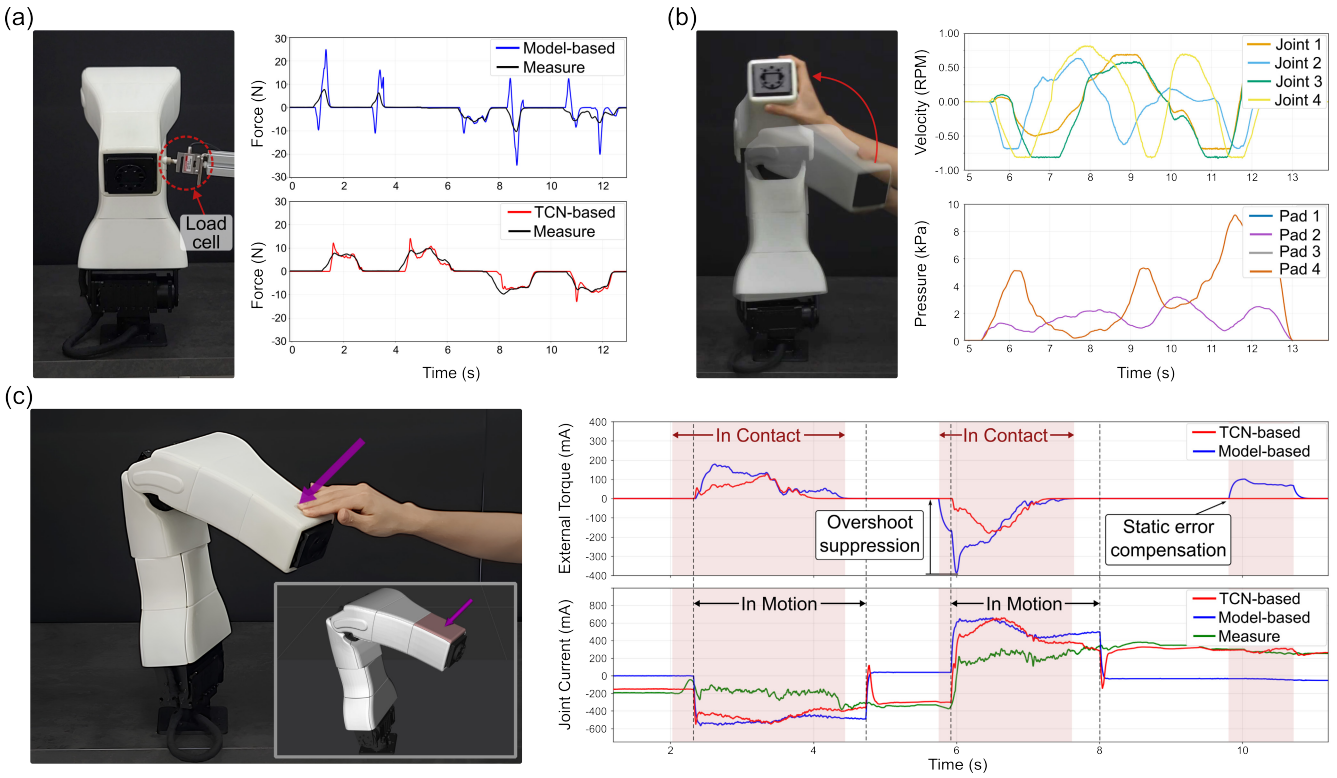

Fig. 6. Demonstration of the TCN-based compensator performance and sensor fusion during physical human-robot interaction scenarios. (a) Comparison of system response during static-to-kinetic transition without and with the TCN compensator; (b) Joint trajectory and pneumatic sensor data during a shear-force-dominant task compliance; (c) Estimated external force and motor torque for Joint 3 in a general kinesthetic teaching scenario, comparing TCN compensator and nominal model responses.

B. Demonstration

Effective kinesthetic teaching demands several key system properties for intuitive pHRI. The system must exhibit low force thresholds and low damping characteristics, enabling the operator to initiate motion with minimal force and sustain teaching without fatigue [27]. Furthermore, the system response must be predictable and consistent, accurately reflecting user intent without overshoot or undershoot. These properties, however, are difficult to achieve using a single sensing modality.

Proprioceptive-based approaches inherently face a trade-off between responsiveness and stability that a dead band set for stability results in poor responsiveness, while lowering damping induces system instability [28].

Conversely, approaches relying solely on tactile data are limited in providing sufficient information for precise task compliance. Although tactile signals are adept at resolving the location and approximate magnitude of discrete contact points, they often fail to adequately account for complex multi-point contact scenarios, such as grasping, where the individual forces distributed across the robot's surface may not align with the net force vector required for the task.

Here we propose proprioceptive-tactile fusion framework that addresses these limitations. The system achieves robust task compliance unattainable by tactile-only sensing, while simultaneously mitigating the responsiveness limitations inherent to proprioceptive methods, thereby providing an intuitive and stable user experience. For validation, we performed a kinesthetic teaching demonstration using admittance control (Fig. 6).

To ensure high responsiveness, we configured a small dead band of 1.5σ ($\sim$86.6%) for all demonstration scenarios, with σ being the standard deviation of the estimation error measured during the static-to-kinetic transition (Table I). Although such a low threshold is generally undesirable for safe pHRI, our robotic skin directly senses contact, providing reliable contact-state estimation and preserving both stability and responsiveness.

The first demonstration compares the force estimation performance of the TCN compensator relative to a nominal model (Fig. 6(a)). The robot executes compliance motion according to the external forces vector, with forces applied using a load cell. To evaluate external force estimation performance during static-to-kinetic transitions, weak and slow forces were applied in short, repeated intervals. Without compensation, applying a force to the robot resulted in significant overshoot and undershoot. In cases where the previous and current force directions were identical, these effects were particularly severe. Incorporating the TCN model eliminated undershoot and substantially reduced overshoot.

To evaluate task compliance during kinesthetic teaching, we guided the robot by firmly grasping the end-effector and executing complex trajectories as presented in Fig. 6(b). In this setting, pneumatic-pad signals vary with contact area and shape, so tactile measurements alone are unreliable for characterizing the interaction. Instead, the proposed sensor-fusion framework estimates the contact location from the pads and maps the resulting joint-level torque to a task-compliance trajectory.

While the previous demo evaluated task compliance in a grasp, the next presents a more general kinesthetic teaching with non-prehensile interactions (Fig. 6(c)). This scenario consists of three sequential contacts. In the second contact, the TCN compensator addresses two issues. First, it removes the static-friction error at contact onset. This error can appear even before motion begins because the dead band is small. Second, it reduces the overshoot that occurs when the motor starts responding to the external force. During the third contact, the compensator again eliminates the static-friction error. In this demonstration, the executed motion follows the compliance trajectory generated by the TCN model, and the nominal model is evaluated by computing its prediction along this TCN-generated motion.

VI. DISCUSSION

In this paper, we present a sensor-fusion method that combines contact information from large-area robotic skin with motor-current data. By exploiting tactile cues, we estimate a static-friction baseline in a model-free manner. We use this baseline (static friction), together with kinematic states, as direct inputs to a temporal convolutional network (TCN) that compensates friction at motion onset. We found that the TCN model reduced the dead-band by 53.86% relative to the uncompensated baseline, thereby improving contact sensitivity. The TCN also mitigated overshoot and undershoot appropriately, suggesting the benefits of the sensor fusion in realizing natural and smooth interaction.

While the TCN mitigates errors at motion onset, it is less reliable during the transition from dynamic motion to static state. Immediately after motion ceases, the friction state is unpredictable, making the estimate of static friction torque $\hat{\tau}_{fric,s}$ unreliable. Nonetheless, this does not compromise stability, because the compliance mode is terminated as the contact disappears. Future work will model this issue more thoroughly.

ACKNOWLEDGMENT

This work was supported in part by the National Research Foundation of Korea (NRF) grant funded by the Korea government (MSIT) (RS-2024-00352818), in part by the NRF grant funded by the MSIT (RS-2025-25448259), in part by Basic Science Research Program through the NRF funded by the Ministry of Education (RS-2025-25420118), and in part by the Institute of Information & Communications Technology Planning & Evaluation (IITP) grant funded by the Korea government (MSIT) (RS-2025-25442149, LG AI STAR Talent Development Program for Leading Large-Scale Generative AI Models in the Physical AI Domain).

REFERENCES

[1] U. E. Ogenyi, J. Liu, C. Yang, Z. Ju, and H. Liu, "Physical human–robot collaboration: Robotic systems, learning methods, collaborative strategies, sensors, and actuators," *IEEE transactions on cybernetics*, vol. 51, no. 4, pp. 1888–1901, 2019.

[2] M. Althoff, A. Giusti, S. B. Liu, and A. Pereira, "Effortless creation of safe robots from modules through self-programming and self-verification," *Science Robotics*, vol. 4, no. 31, p. eaaw1924, 2019.

[3] M. Iskandar, O. Eiberger, A. Albu-Schäffer, A. De Luca, and A. Dietrich, "Collision detection, identification, and localization on the dlr sara robot with sensing redundancy," in *2021 IEEE international conference on robotics and automation (ICRA)*. IEEE, 2021, pp. 3111–3117.

[4] S. K. Kommuri, S. Han, and S. Lee, "External torque estimation using higher order sliding-mode observer for robot manipulators," *IEEE/ASME Transactions on Mechatronics*, vol. 27, no. 1, pp. 513–523, 2021.

[5] S. K. Das, M. N. Saadatzi, S. Abubakar, and D. O. Popa, "Joint torque estimation using base force-torque sensor to facilitate physical human-robot interaction (phri)," in *2019 IEEE 15th International Conference on Automation Science and Engineering (CASE)*. IEEE, 2019, pp. 1367–1372.

[6] J. Choi, S. Kang *et al.*, "External force estimation using joint torque sensors for a robot manipulator," in *2012 IEEE International Conference on Robotics and Automation*. IEEE, 2012, pp. 4507–4512.

[7] S.-D. Lee, M.-C. Kim, and J.-B. Song, "Sensorless collision detection for safe human-robot collaboration," in *2015 IEEE/RSJ International Conference on Intelligent Robots and Systems (IROS)*. IEEE, 2015, pp. 2392–2397.

[8] B. Xu, P. Xu, and B. Li, "Ladrc-based sensorless force control for robotic joint considering static friction," *IEEE Transactions on Instrumentation and Measurement*, 2024.

[9] A. Wahrburg, J. Bös, K. D. Listmann, F. Dai, B. Matthias, and H. Ding, "Motor-current-based estimation of cartesian contact forces and torques for robotic manipulators and its application to force control," *IEEE Transactions on Automation Science and Engineering*, vol. 15, no. 2, pp. 879–886, 2017.

[10] Y. Wei, S. Lyu, W. Li, X. Yu, Z. Wang, and L. Guo, "Contact force estimation of robot manipulators with imperfect dynamic model: On gaussian process adaptive disturbance kalman filter," *IEEE Transactions on Automation Science and Engineering*, vol. 21, no. 3, pp. 3524–3537, 2023.

[11] S. Shan and Q.-C. Pham, "Sensorless estimation of contact using deep-learning for human-robot interaction," in *2024 IEEE International Conference on Robotics and Automation (ICRA)*. IEEE, 2024, pp. 12 935–12 941.

[12] J. Shim, S. Lee, D. Jeon, and J.-I. Ha, "Contact force estimation using uncertain torque model and friction models for robot manipulator," *IEEE Transactions on Industrial Electronics*, vol. 71, no. 10, pp. 12 634–12 644, 2024.

[13] H. Hu, Z. Shen, and C. Zhuang, "A pinn-based friction-inclusive dynamics modeling method for industrial robots," *IEEE Transactions on Industrial Electronics*, 2024.

[14] G. Cheng, E. Dean-Leon, F. Bergner, J. R. G. Olvera, Q. Leboutet, and P. Mittendorfer, "A comprehensive realization of robot skin: Sensors, sensing, control, and applications," *Proceedings of the IEEE*, vol. 107, no. 10, pp. 2034–2051, 2019.

[15] K. Park, H. Yuk, M. Yang, J. Cho, H. Lee, and J. Kim, "A biomimetic elastomeric robot skin using electrical impedance and acoustic tomography for tactile sensing," *Science Robotics*, vol. 7, no. 67, p. eabm7187, 2022.

[16] L. Van Duong and V. A. Ho, "Large-scale vision-based tactile sensing for robot links: Design, modeling, and evaluation," *IEEE Transactions on Robotics*, vol. 37, no. 2, pp. 390–403, 2021.

[17] G. Pang, G. Yang, W. Heng, Z. Ye, X. Huang, H.-Y. Yang, and Z. Pang, "Coboskin: Soft robot skin with variable stiffness for safer human–robot collaboration," *IEEE Transactions on Industrial Electronics*, vol. 68, no. 4, pp. 3303–3314, 2021.

[18] J. A. Barreiros, A. Ö. Önol, M. Zhang, S. Creasey, A. Goncalves, A. Beaulieu, A. Bhat, K. M. Tsui, and A. Alspach, "Learning contact-rich whole-body manipulation with example-guided reinforcement learning," *Science Robotics*, vol. 10, no. 105, p. eads6790, 2025.

[19] K. Park, K. Shin, S. Yamsani, K. Gim, and J. Kim, "Low-cost and easy-to-build soft robotic skin for safe and contact-rich human–robot collaboration," *IEEE Transactions on Robotics*, vol. 40, pp. 2327–2338, 2024.

[20] F. Nori, S. Traversaro, J. Eljaik, F. Romano, A. Del Prete, and D. Pucci, "icub whole-body control through force regulation on rigid non-coplanar contacts," *Frontiers in Robotics and AI*, vol. 2, p. 6, 2015.

[21] E. Magrini, F. Flacco, and A. De Luca, "Estimation of contact forces using a virtual force sensor," in *2014 IEEE/RSJ International Conference on Intelligent Robots and Systems*. IEEE, 2014, pp. 2126–2133.

[22] Y. Tian, C. Guang, R. Luo, S. Bao, J. Yuan, L. Du, and Z. Hu, "Contact force estimation by fusing current and tactile information through kf for robot arm," in *2024 IEEE International Conference on Robotics and Biomimetics (ROBIO)*. IEEE, 2024, pp. 2259–2264.

[23] M. Iskandar and S. Wolf, "Dynamic friction model with thermal and load dependency: modeling, compensation, and external force estimation," in *2019 International Conference on Robotics and Automation (ICRA)*. IEEE, 2019, pp. 7367–7373.

[24] C. C. De Wit, H. Olsson, K. J. Astrom, and P. Lischinsky, "A new model for control of systems with friction," *IEEE Transactions on automatic control*, vol. 40, no. 3, pp. 419–425, 1995.

[25] F. Al-Bender, V. Lampaert, and J. Swevers, "The generalized maxwell-slip model: a novel model for friction simulation and compensation," *IEEE Transactions on automatic control*, vol. 50, no. 11, pp. 1883–1887, 2005.

[26] J. Kim, D. C. Mathur, K. Shin, and S. Taylor, "Papras: Plug-and-play robotic arm system," *arXiv preprint arXiv:2302.09655*, 2023.

[27] J. Chen and P. I. Ro, "Human intention-oriented variable admittance control with power envelope regulation in physical human-robot interaction," *Mechatronics*, vol. 84, p. 102802, 2022.

[28] L. Han, L. Zhao, Y. Huang, and W. Xu, "Variable admittance control for safe physical human–robot interaction considering intuitive human intention," *Mechatronics*, vol. 97, p. 103098, 2024.